PCCP

Accepted Manuscript

This is an *Accepted Manuscript*, which has been through the Royal Society of Chemistry peer review process and has been accepted for publication.

Accepted Manuscripts are published online shortly after acceptance, before technical editing, formatting and proof reading. Using this free service, authors can make their results available to the community, in citable form, before we publish the edited article. We will replace this *Accepted Manuscript* with the edited and formatted *Advance Article* as soon as it is available.

You can find more information about *Accepted Manuscripts* in the Information for Authors.

Please note that technical editing may introduce minor changes to the text and/or graphics, which may alter content. The journal's standard Terms & Conditions and the Ethical guidelines still apply. In no event shall the Royal Society of Chemistry be held responsible for any errors or omissions in this *Accepted Manuscript* or any consequences arising from the use of any information it contains.

ROYAL SOCIETY OF CHEMISTRY

www.rsc.org/pccp

Crystal Plane-Dependent Gas-Sensing Properties of Zinc Oxide Nanostructures: Experimental and Theoretical Studies

Yusuf V. Kaneti,[a] Zhengjie Zhang,[a] Jeffrey Yue,[b] Quadir M.D. Zakaria,[a] Chuyang Chen,[a] Xuchuan Jiang,[a,*] and Aibing Yu[a]

[a]*School of Materials Science and Engineering, The University of New South Wales, Sydney NSW 2052, Australia*

[b]*Department of Chemical Engineering, University College London, Torrington Place, London WC1E 7JE, United Kingdom.*

Abstract

The sensitivity of a metal oxide gas sensor is strongly dependent on the nature of the crystal surface exposed to the gas species. In this study, two types of zinc oxide (ZnO) nanostructures: nanoplates and nanorods with exposed (0001) and $(10\bar{1}0)$ crystal surfaces, respectively, were synthesized through facile solvothermal methods, respectively. The gas-sensing results show that sensitivity of the ZnO nanoplates toward ethanol is two times higher than that of the ZnO nanorods, at an optimum operating temperature of 300 ºC. This could be attributed to the higher surface area and the exposed (0001) crystal surfaces. DFT (Density Functional Theory) simulations were carried out to study the adsorption of ethanol on the ZnO crystal planes such as (0001), $(10\bar{1}0)$, and $(11\bar{2}0)$ with adsorbed O^- ion. The results reveal that the exposed (0001) planes of the ZnO nanoplates promote better ethanol adsorption by interacting with the surface oxygen *p* (O2*p*) orbitals and stretching the O-H bond to lower the adsorption energy, leading to the sensitivity enhancement of the nanoplates. The findings will be useful for the fabrication of metal

* To whom correspondence should be addressed. Email: xcjiang@unsw.edu.au. Tel: +61-2-9385 5918.

Physical Chemistry Chemical Physics Accepted Manuscript

oxide nanostructures with specifically exposed crystal surfaces for improved gas-sensing and/or catalytic performance.

Keywords: Zinc oxide, Gas sensors, Density functional theory, Nanorods, Nanoplates, Exposed surface, Ethanol

1. Introduction

Zinc oxide (ZnO), an *n*-type semiconductor with a wide band-gap (E_g) of 3.37 eV, has attracted considerable attention because of its unique optical and electronic properties and potential applications in solar cells,[1] nanolasers,[2] nanogenerators,[3] catalysts,[4] environmental remediation[5], and gas sensors.[6] Recently, there has been a growing interest in the synthesis of metal oxide nanostructures with specifically exposed crystal planes and the exploration of their crystal plane-dependent properties, in applications such as gas sensors and catalysts.[7-12] For example, Han et al.[13] reported that WO_3 nanoparticles exhibiting a higher percentage of (010) than (001) or (100) planes showed an enhanced sensitivity toward 1-butylamine. Similarly, SnO_2 octahedral nanoparticles with exposed high energy planes such as {221} or {111} were found to exhibit enhanced sensitivities toward ethanol (EthOH) compared to SnO_2 nanorods enclosed with lower energy {101} and {110} planes.[7] Lai et al.[10] demonstrated that TiO_2 nanomaterials with exposed (111) and (001) planes exhibited 5 times higher photoreactivity than those with exposed (110) facets.

In order to a achieve a better understanding of the sensing mechanism of ZnO-based sensors, some theoretical studies have been conducted to investigate the adsorption of oxidizing gases (e.g. NO_2, NO, SO_2) on the surfaces of ZnO.[14-17] For instance, Breedon et al.[14, 18] investigated the adsorption of NO and NO_2 onto stoichiometrically balanced ZnO($10\bar{1}0$) and ($2\bar{1}\bar{1}0$) crystal planes by using DFT simulation

Physical Chemistry Chemical Physics Accepted Manuscript

method and found that NO_2 and NO interacted weakly with the two crystal planes without generating any significant surface distortions. Prades et al.[16] examined the adsorption of NO_2 on ZnO($10\bar{1}0$) and ($11\bar{2}0$) crystal planes with slightly reduced (12.5 % O vacancy) by using DFT simulations and demonstrated that NO_2 strongly adsorbed on the surface Zn atoms. In comparison, only few studies were reported on the adsorption of reducing gases (e.g. CO, alcohols) on the crystal planes of ZnO.[19, 20] Recently, our group have employed molecular dynamics (MD) simulation method to quantify the diffusivity, adsorption, and reaction capabilities of volatile *n*-butanol gas on the ZnO($10\bar{1}0$), ($11\bar{2}0$), and (0001) planes.[20]

Despite some success, many of the previous investigations were still limited to the exploration of one particular ZnO crystal surface, which provide only partial information about the sensing mechanism of ZnO-based sensors on atomic/molecular scale. Moreover, the electronic interactions that occur between EthOH and O^- modified ZnO crystal surfaces during the gas-sensing process are not yet fully understood, specifically for a few aspects such as: (i) changes in electronic states and adsorption energies of the ZnO crystal planes before and after interacting with EthOH molecules, (ii) the impact of the interaction on the bond length of the EthOH molecules, (iii) the electron/charge distribution on the ZnO surfaces after EthOH adsorption, and (iv) the adsorption mechanism of EthOH molecules on the ZnO surfaces.

This study aims to develop a facile hydrothermal or solvothermal process for the synthesis of ZnO nanostructures with exposed ($10\bar{1}0$) and (0001) crystal planes for gas-sensing application, using EthOH as a case study. The crystal plane-dependent gas-sensing properties of the as-prepared ZnO nanoplates and nanorods will be examined, both experimentally and theoretically. To fundamentally understand the

Physical Chemistry Chemical Physics Accepted Manuscript

sensing mechanisms, DFT simulations will be employed to quantify the changes in density of states (DOS), adsorption energies, and bond angles or distances, on different ZnO crystal surfaces (i.e. $10\bar{1}0$), ($11\bar{2}0$), and (0001) surfaces) modified with adsorbed O^-, before and after interaction with EthOH. The findings will provide a greater understanding of the sensing mechanism of ZnO-based sensors on atomic/molecular scale and will be beneficial for the fabrication of other metal oxide nanomaterials with highly exposed crystal surfaces for potential applications in gas sensors and catalysis.

2. Experimental Section

2.1 Chemicals

The chemicals used in this study are zinc chloride ($ZnCl_2$, 99 %), zinc acetate dehydrate ($Zn(CH_3COO)_2.2H_2O$, 99%), sodium hydroxide (NaOH, 99%), sodium acetate ($NaC_2H_3O_2$, 99%), ethanol (C_2H_6O, 95%), (absolute ethanol (C_2H_6O, 99.9%), and cetyltrimethylammonium bromide (CTAB, 99%), 1-methyl-2-pyrrolidinone (C_5H_9NO, 99.5%), and polyvinylidene fluoride $(CH_2CF_2)_n$, 99.5%). All chemicals were purchased from Sigma Aldrich and used as received without further purification. Distilled water was used in all the synthesis processes.

2.2 Synthesis of ZnO nanostructures

***ZnO hexagonal nanoplates*:** ZnO hexagonal nanoplates with exposed (0001) were synthesized by using a modified solvothermal process.[21] In a typical protocol, 0.66 g of $Zn(CH_3COO)_2.2H_2O$, 0.24 g of NaOH, and 1.6 g of $NaCH_3COO$, were successively dissolved in a water (20 mL)/ethanol (10 mL) mixed solvent. The white suspension was stirred for ~20 minutes and then transferred into a 50 mL Teflon-lined stainless steel autoclave, which was sealed and maintained at 150 °C for 24 h. Finally, it

Physical Chemistry Chemical Physics Accepted Manuscript

was cooled to room temperature naturally and the white precipitates were collected, rinsed with deionized water and ethanol for 3 times along with centrifugation, and dried at 60 °C for 5 h.

***ZnO nanorods*:** In a typical procedure, a 2 mL solution of $ZnCl_2$ (0.05 M) was firstly mixed with a 40 ml of NaOH (0.15 M) solution. Then, 2 mmol of CTAB powder was added to the mixture solution to form a white suspension, followed by rapid stirring for ~20 minutes. This suspension was subsequently transferred into a 50 mL Teflon-lined stainless steel autoclave, and finally sealed and heated at 150 °C for 16 h. The washing procedures were similar to those described for ZnO hexagonal nanoplates.

2.3 Characterization

Field emission scanning electron microscopy (FESEM) analysis of the ZnO samples was performed using a FEI Nova NanoSEM 230. Transmission electron microscopy (TEM) images were obtained using a Tecnai G^2 microscope operated at an accelerating voltage of 200 kV. High resolution transmission electron microscopy (HRTEM) was performed using a Phillips CM200 field emission gun transmission electron microscope with an acceleration voltage of 200 kV. The crystal structures of the as-prepared ZnO products were characterized using X-ray diffraction (Phillips X'pert multipurpose X-ray diffraction system (MPD) equipped with graphite mono-chromatized Cu Kα radiation (λ = 1.54 Å)) in the 2θ range of 20-70°. X-ray photoelectron spectra (XPS) were recorded on an ESCALAB250Xi X-ray photoelectron spectrometer, using Al-Kα radiation as the exciting source. The Brunauer–Emmett–Teller (BET) surface area and pore size distribution of the products were obtained from nitrogen physisorption isotherms (adsorption–desorption branches) at 77 K on a Micromeritics Tristar 3000 instrument. Prior to the measurements, the ZnO samples were degassed overnight under vacuum at 150 °C to vaporize water molecules adsorbed on the ZnO materials.

Physical Chemistry Chemical Physics Accepted Manuscript

Physical Chemistry Chemical Physics Accepted Manuscript

2.4 Gas sensor fabrication

To prepare the gas sensor, each ZnO product was mixed and ground with polyvinylidene fluoride (PVDF) and 1-methyl-2-pyrollidone in an agate mortar. The resulting paste was spread uniformly onto an alumina ceramic tube with a pair of previously-printed Au electrodes. The coated ceramic tube was subsequently aged at 450 °C for a period of 3 h to improve its thermal stability. Finally a Ni-Cr alloy coil was inserted into the alumina tube as a heater, which provided the working temperature of the gas sensor. The gas-sensing tests were performed on a WS-30A gas sensing measurement system (Weisheng Electronics Co., Ltd., Henan, China) at a relative humidity of about 40-60% and a working voltage of 5 V, with a reference resistor of 1MΩ, using air as the dilution and reference gas.

For the gas-sensing tests, a static state gas-distribution method was used, as shown in Fig. S2. Firstly, the sensors were pre-heated to ensure stable data collection due to the moisture adsorbed on the materials. Once, the sensors were stabilized, a calculated volume of the test gas was injected into the glass-inlet at the back of the chamber using a micro-syringe and dropped onto a small hot-plate located inside the chamber. To achieve a certain concentration of ethanol vapor, the amount of liquid ethanol (99.9% purity) that needed to be injected was calculated according to the equation:

$$V_{liquid} = (V_{chamber} \times 1000 \times C_{gas} \times M.W_{gas} \times T_{room} \times 10^{-9}) / (22.4 \times \rho_{liquid} \times T_{surrounding}) \quad (1)$$

where V_{liquid} is the volume of liquid ethanol to be injected (μL), $V_{chamber}$ is the total volume of the chamber (18 L), C_{gas} is the concentration of ethanol gas (ppm), $M.W_{gas}$ is the molecular weight of ethanol gas, T_{room} is the room temperature (298 K), ρ_{liquid} is the density of liquid ethanol (g/cm^3), and $T_{surrounding}$ is the surrounding temperature (K).

As the injected gas was initially in the liquid form, it was evaporated to convert it to a gas state. Once the maximum sensitivity of the sensors was reached, the chamber was opened in order to release the gas or to allow the sensors to recover. During the gas-sensing measurements, the operating temperature was controlled by adjusting the heating voltage. The sensitivity (S) of the sensor is defined as: $S = R_a/R_g$, where R_a and R_g correspond to the resistance of the sensor in air and the resistance in the tested gas, respectively. The response time (τ_{res}) is defined as the time required for the conductance variation of the sensor to reach 90% of its equilibrium value, following exposure to ethanol vapor. The recovery time (τ_{rec}) is defined as the time needed by the sensor to return to 10% of its original conductance in air, after removal of the ethanol vapor. The digital photographs of the prepared ZnO sensors are given in Fig. S3.

2.5 Computational simulations

Density Functional Theory (DFT) simulations were conducted using the commercial software: Materials Studio (Version 4.3, Accelrys Inc, 2007) with the CASTEP[22] module and the widely used GGA (generalized gradient approximation) for the exchange-correlation using PBE (Perdew, Burke, and Emzerhof). The self-consistent ground state cell optimization was performed by density mixing scheme using an ultra-soft pseudo-potentials (USP) plane-wave basis set, with a cut-off energy of 400 eV and thermal broadening of 0.1 eV. The Monkhorst-Pack was used to determine the *k*-points, which was fixed at 0.04 $Å^{-1}$ for all calculations.

The surface simulations were performed using a slab model with periodic boundary conditions (Scheme 1). A supercell with surface thickness of ~10 Å and vacuum space of 20 Å was created from the ZnO lattice structure in which the bottom layers (~6 Å) were fixed and the top layers were relaxed to simulate the surface properties. In order to simulate the gas sensing environment as close as possible, one O^- ion

Physical Chemistry Chemical Physics Accepted Manuscript

was bonded with the surface Zn atom on the optimized ZnO surface. Then, the EthOH molecule was positioned ~2.0 Å from the surface above different adsorption surfaces.

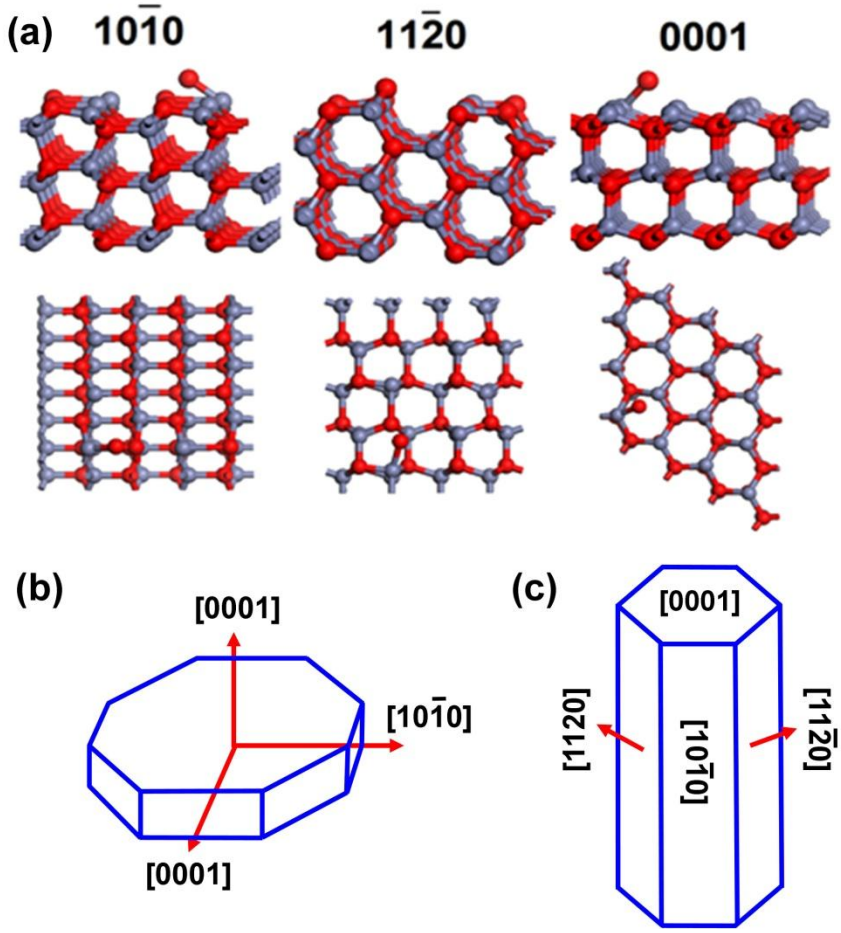

Scheme 1. (a) Side view (top) and top view (bottom) of the three different ZnO crystal surfaces (red and blue atoms represent O and Zn, respectively); schematic illustration of the crystal faces in: (b) ZnO hexagonal nanoplates, and (c) ZnO nanorods.

The adsorption energy values of EthOH molecule to different surfaces were calculated using the following formula:

$$E_{ads} = [E_{(EthOH/ZnO)} - (E_{EthOH} + E_{ZnO})] \quad (1)$$

Physical Chemistry Chemical Physics Accepted Manuscript

where E_{ads} is the adsorption energy, $E_{(EthOH/ZnO)}$ is the total energy after adsorption, E_{EthOH} is the total energy of the EthOH molecule, and E_{ZnO} is the total energy of three bare ZnO surfaces after optimization. A negative binding energy indicates favorable adsorption and the more negative the value, the stronger the adsorption capability.

3. Results and Discussion

3.1 Composition and morphology

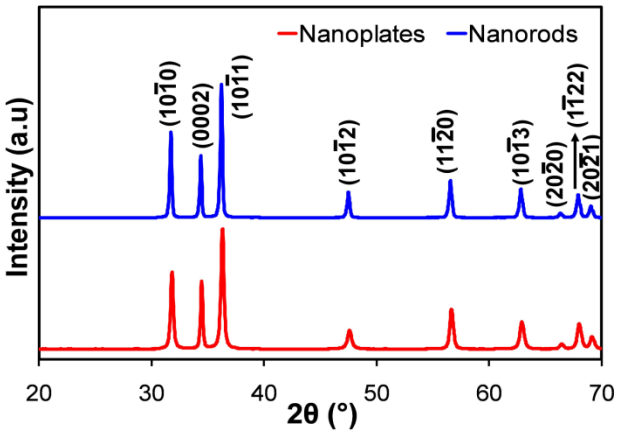

Fig. 1 XRD patterns of the as-prepared ZnO nanoplates and nanorods.

The phase composition of the achieved products was characterized using XRD technique as shown in Fig. 1. All of the diffraction peaks in both products can be well indexed to hexagonal wurtzite ZnO (JCPDS No. 36-1451). Furthermore, the absence of diffraction peaks due to impurities in both ZnO samples indicates their high purity. The sharp, clear distinct peaks observed in the XRD patterns of these two samples suggest that the as-synthesized ZnO nanostructures are well-crystallized.

Fig. 2a and b shows the SEM images of the as-prepared ZnO nanoplates, which have diameters of 100-150 nm and are hexagonal-like. The HRTEM analysis of an individual hexagonal nanoplate (Fig. 3b)

Physical Chemistry Chemical Physics Accepted Manuscript

reveals clear lattice fringes, with a *d*-spacing of ~0.28 nm, which corresponds well to the *d*-spacing of $(10\bar{1}0)$ plane of the hexagonal wurtzite ZnO. The selected area electron diffraction (SAED) pattern of the ZnO hexagonal nanoplates shown in Fig. 3c can be indexed to [0001] zone-axis of single crystal hexagonal wurtzite ZnO. The HRTEM and the corresponding SAED results of the nanoplates reveal that the they grow mainly along six symmetric directions of ± $[10\bar{1}0]$, ±$[1\bar{1}00]$, and ±$[01\bar{1}0]$. Therefore, the top and bottom surfaces of the nanoplates expose ±(0001) planes, as represented by Scheme 1b.[20]

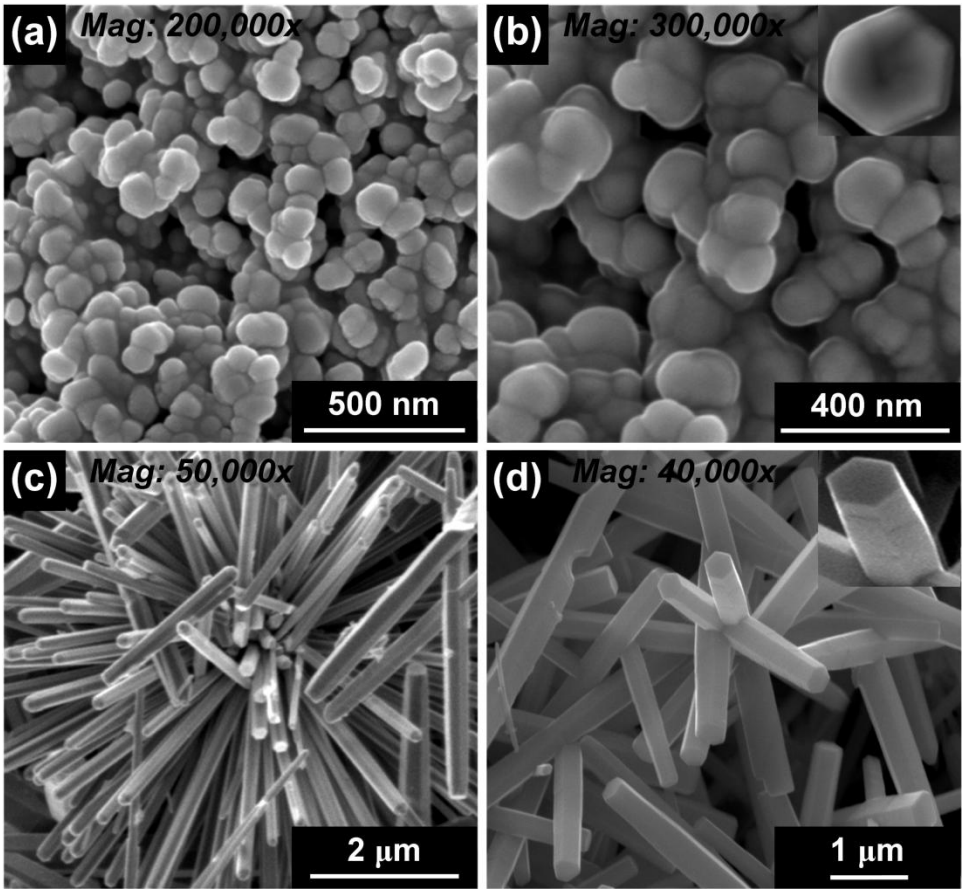

Fig. 2 Low and high magnification SEM images of (a, b) ZnO nanoplates and (c, d) ZnO nanorods.

In comparison, the as-prepared ZnO nanorods have lengths and diameters of ~1-2.5 μm and ~200-400 nm, respectively, as shown in Fig. 2c and d. The HRTEM image of a single nanorod (Fig. 3e) shows distinct lattice fringes with a *d*-spacing of ~0.26 nm, corresponding to the *d*-spacing of the (0001) plane

Physical Chemistry Chemical Physics Accepted Manuscript

of the hexagonal wurtzite ZnO. Furthermore, it is observed that the identified (0001) plane is perpendicular to the axis of the nanorods, suggesting that the preferred growth of the nanorods is along the [0001] direction.[23-25] The SAED pattern of the ZnO nanorods shown in Fig. 3f can be ascribed to diffraction pattern of [10$\bar{1}$0] zone axis of the hexagonal wurtzite ZnO. This indicates that the ZnO nanorods expose the (10$\bar{1}$0) planes, as schematically illustrated in Scheme 1c.

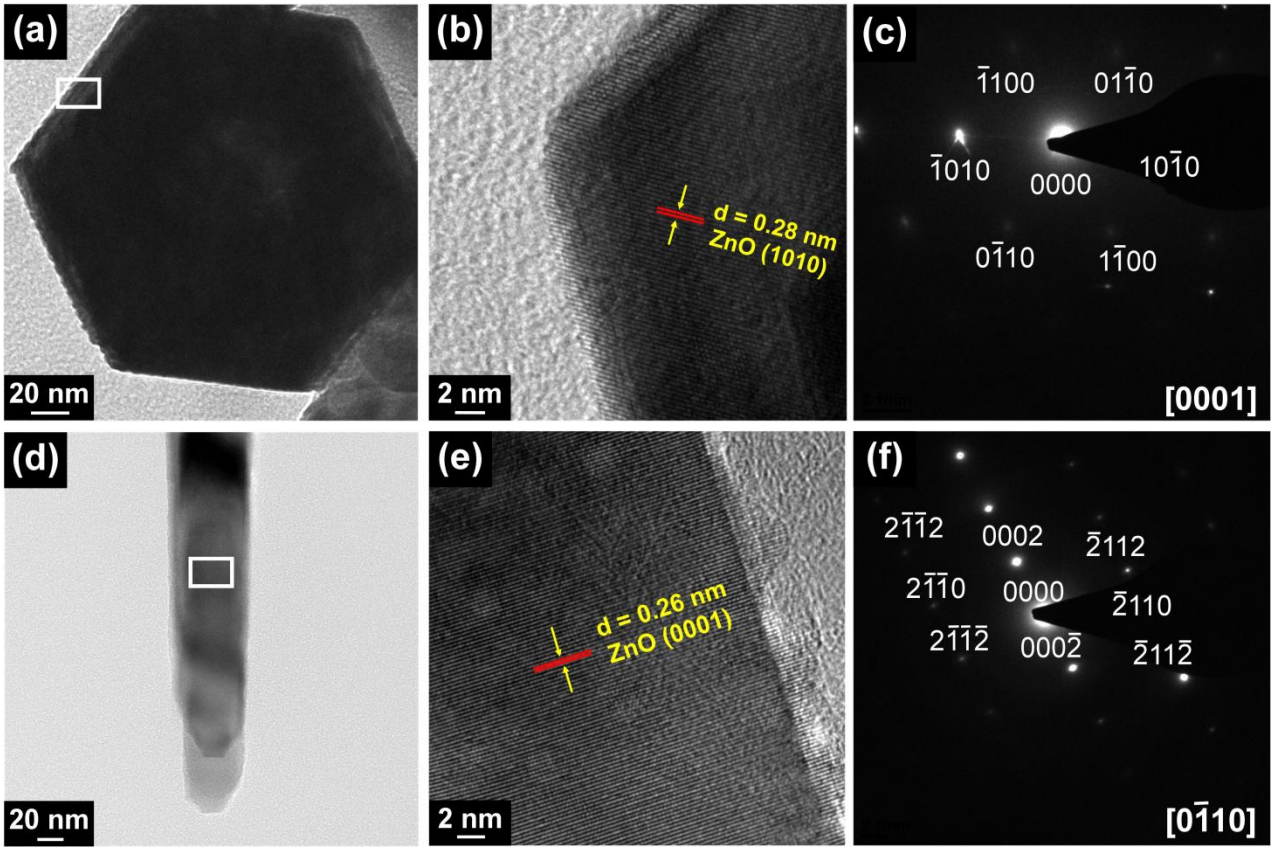

Fig. 3 TEM and HRTEM images and the corresponding SAED pattern of an individual (a, b, c) ZnO nanoplate, and (d, e, f) ZnO nanorod.

In the present reaction system, the formation of ZnO crystals initially originates from the reaction between Zn^{2+} (from $ZnCl_2$ in the case of ZnO nanorods or $Zn(CH_3COO)_2$ for the ZnO nanoplates) and OH^-, which generates the precursor zinc hydroxide, $Zn(OH)_2$. The formed $Zn(OH)_2$ precipitate, can

Physical Chemistry Chemical Physics Accepted Manuscript

subsequently be dissolved by the superfluous OH^- ions present in the solution to generate $[Zn(OH)_4]^{2-}$ ions, which have been proposed to be the growth units of ZnO.[26] As the solution is heated to high temperature, ZnO clusters are formed from the dehydration or decomposition of $[Zn(OH)_4]^{2-}$ ions. Eventually, the solution reaches supersaturation from the formation of these clusters and nucleation begins, followed by the crystal growth.

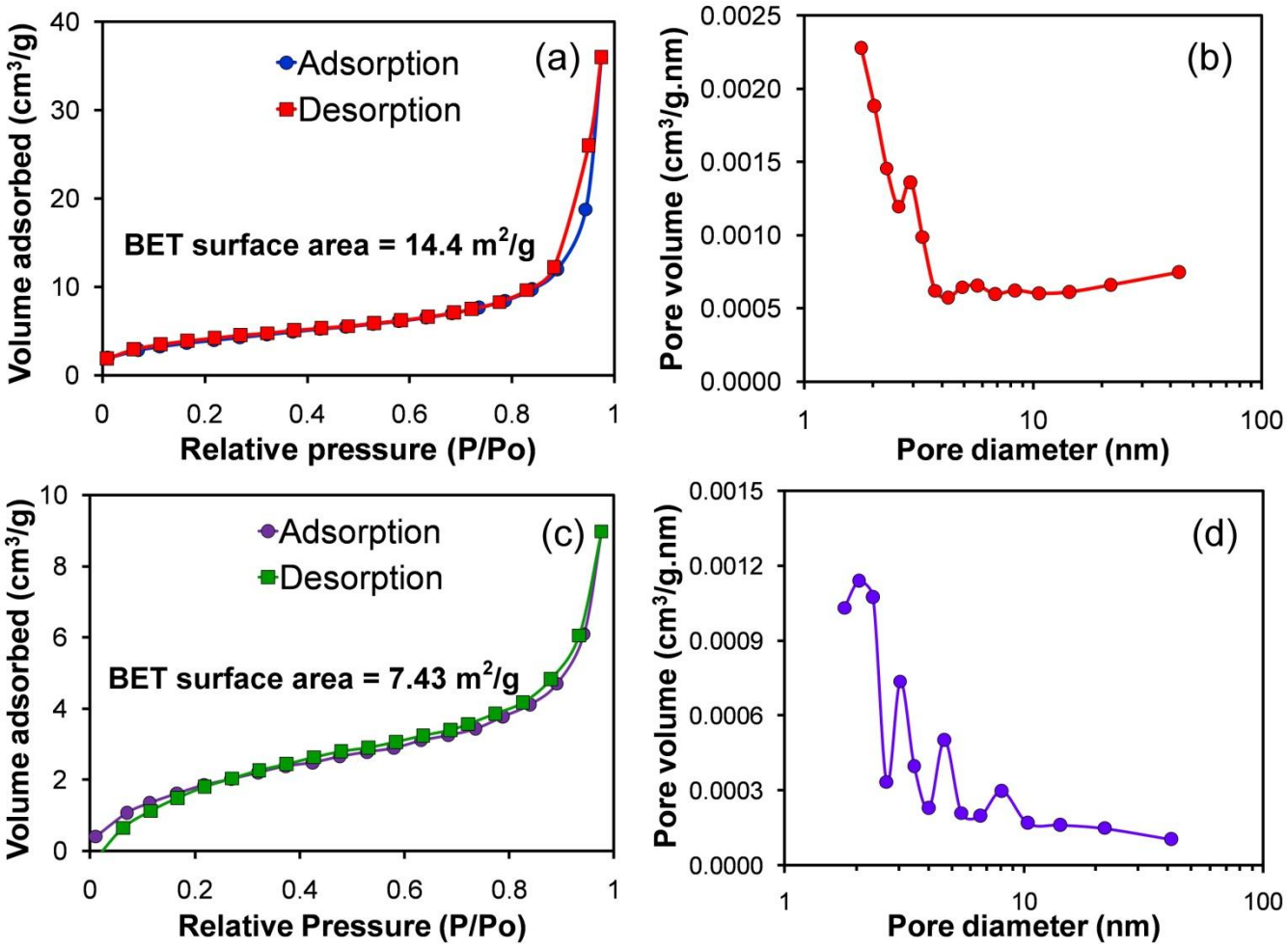

Fig. 4 The nitrogen (N_2) adsorption-desorption isotherms of (a) ZnO hexagonal nanoplates and (b) ZnO nanorods.

The crystal structure of hexagonal wurtzite ZnO is composed of positively charged Zn-(0001) and negatively charged O-$(000\bar{1})$ polar surfaces. Intrinsically, the rate of crystal growth of ZnO is in the

Physical Chemistry Chemical Physics Accepted Manuscript

order: [0001] >> [$10\bar{1}0$] >> [$000\bar{1}$] as the surface energy of the (0001) plane is higher than those of ($10\bar{1}0$) and ($000\bar{1}$) planes.[27] Hence, in the absence of surfactants or other capping agents, ZnO crystal has a strong tendency to grow along the [0001] direction or *c*-axis. Previously, the hydroxyl (OH^-) ion has been identified to preferentially adsorb on the (0001) plane of ZnO at a high concentration level.[28] For the synthesis of ZnO nanorods, a low Zn^{2+}: OH^- ratio is used, and therefore only few growth units, $[Zn(OH)_4]^{2-}$, are generated and the intrinsic growth habit of the ZnO crystal along the [0001] direction cannot be well suppressed by the OH^- ions. This results in a much faster growth rate along the [0001], ultimately leading to the formation of nanorods. On the contrary, in the synthesis of ZnO hexagonal nanoplates, the acetate ions (CH_3COO^-) which are present in high concentration can preferentially adsorb on the (0001) plane of ZnO, in conjunction with the adsorbed hydroxyl ions.[21] As a result, the intrinsically fast growth rate of the ZnO crystal along the [0001] direction is greatly suppressed by the adsorption of CH_3COO^- and OH^- ions on the (0001) plane, while the lateral growth along the [$10\bar{1}0$] direction remains uninhibited and is therefore faster, resulting the formation of two-dimensional nanoplates (Fig.2a and b)

Surface area is one of the key factors influencing the gas-sensing performance of metal oxide gas sensors. The surface areas of the as-prepared ZnO nanostructures were evaluated by the BET method using N_2 adsorption-desorption processes. The BET specific surface area of the ZnO nanoplates is measured to be 14.4 m^2/g, approximately twice of that of the ZnO nanorods (7.43 m^2/g), as shown in Fig. 4. The larger surface area of the nanoplates may provide more sites for the adsorption of O_2 molecules, which play an important role in the sensing mechanism of ZnO-based sensor. XPS technique was employed to gain further information regarding the surface composition and features of the as-prepared ZnO nanostructures. Fig. S4a compares the high resolution spectra of the Zn 2p peaks of both the ZnO

Physical Chemistry Chemical Physics Accepted Manuscript

nanorods and hexagonal nanoplates. It can be observed that the position of Zn 2p peak is nearly identical for the two ZnO samples with the Zn 2p peak located at a binding energy of 1020.98 eV for the ZnO nanoplates and at 1021.68 eV for the ZnO nanorods. This confirms the Zn^{2+} valency state in the prepared ZnO products.[29]

Table 1 Results of Gaussian fitting of O 1s spectra of ZnO nanoplates and nanorods

Samples	**Zn 2p**	**O_L (Zn-O)**	**O_V (vacancy)**	**O_C (chemisorbed)**
ZnO nanoplates				
Binding energy (eV)	1021.41	530.28	531.56	532.3
Relative percentage (%)		75.1	15.6	9.3
ZnO nanorods				
Binding energy (eV)	1021.37	530.24	531.56	532.42
Relative percentage (%)		71.0	21.0	8.0

As shown in Fig. S4b and c, the O1s XPS peak of both ZnO nanostructures can be deconvoluted into three main components after Gaussian fitting: O_L which corresponds to the O^{2-} ions in the ZnO crystal, O_V which is indexed to the O^{2-} ions in the oxygen-deprived areas within the ZnO crystal lattice, and O_C which represents chemisorbed oxygen species.[23] The binding energies of these oxygen components are given in Table 1. The relative percentages of the O_C component in the two ZnO samples are 9.3% for the ZnO nanoplates and 8.0% for the ZnO nanorods, suggesting the higher capability of the nanoplates to absorb more oxygen species compared to the nanorods. These results can be used to understand the shape-dependent gas-sensing performance of ZnO nanostructures.

Physical Chemistry Chemical Physics Accepted Manuscript

3.2 Gas-sensing performance

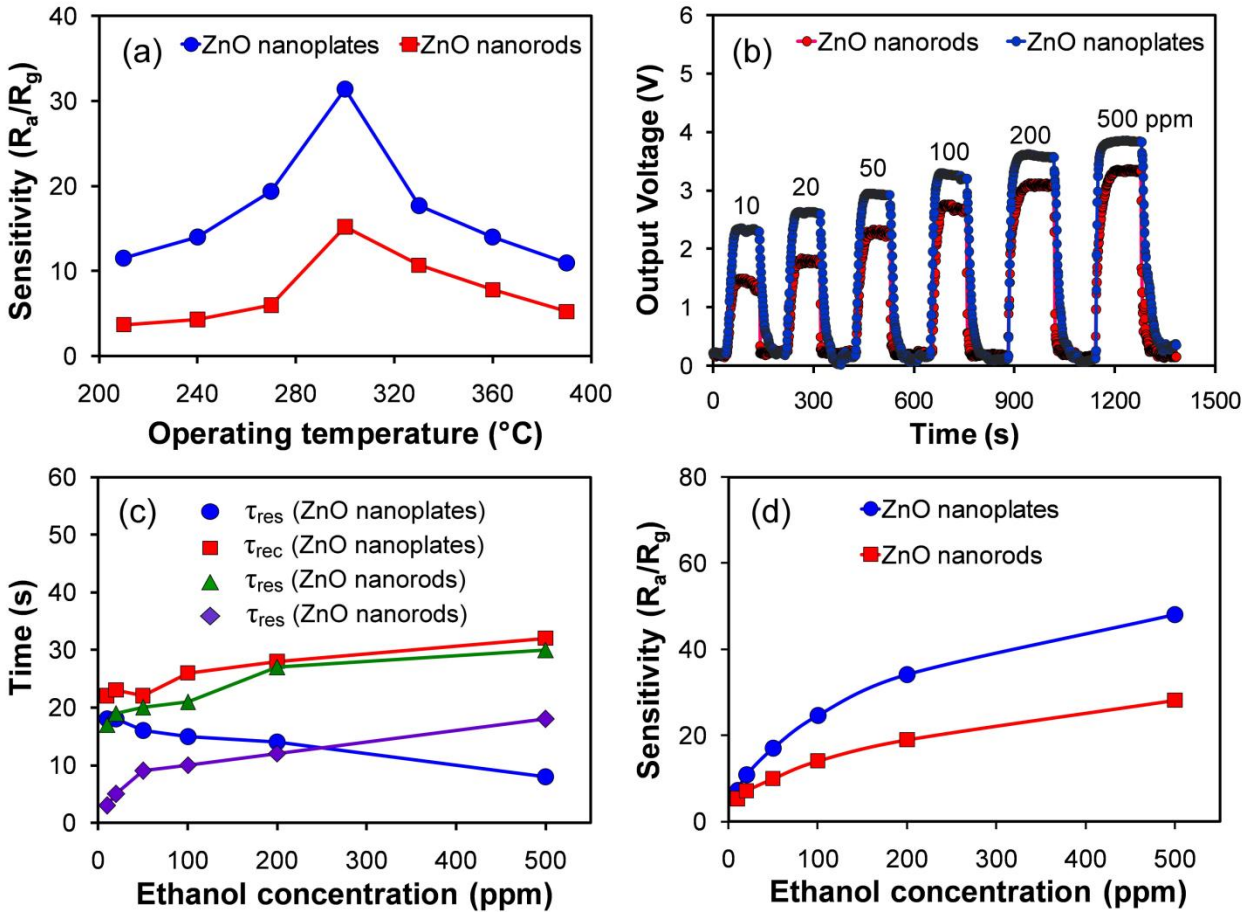

Fig. 5 (a) The sensitivities of the as-prepared ZnO hexagonal nanoplates and nanorods toward 100 ppm of EthOH as a function of the working temperature; (b) the dynamic response-recovery curves; (c) the response-recovery times of the sensors made from the as-prepared ZnO nanostructures on exposure to different concentrations of EthOH at the optimum working temperature of 300 °C; (d) comparison of the sensitivities of the ZnO hexagonal nanoplates and nanorods toward various concentrations of EthOH at 300 °C.

The ZnO nanorods and hexagonal nanoplates exhibit different surface properties (different surface areas, exposed crystal planes, and O_C percentages), which may lead to different gas-sensing properties. As a case study, their sensitivities toward EthOH were investigated in this work. The gas-sensing properties

Physical Chemistry Chemical Physics Accepted Manuscript

of ZnO sensors are heavily affected by the working temperature[14, 30] Therefore, the sensitivities of the as-prepared ZnO nanostructures toward 100 ppm of EthOH were evaluated as a function of working temperature. From Fig. 5a, it can be observed that the sensitivity of the ZnO nanoplate sensor increases gradually with the rise in the working temperature from 210 to 300 °C and reaches a maximum value of S= 24.6 at an optimum working temperature of 300 ºC. Further increase in the operating temperature above 300 °C, however results in a gradual decline in the sensitivity of the ZnO nanoplates. A similar trend is observed for the ZnO nanorods. That is, the optimized working temperatures for both ZnO sensors are 300 °C, however, they exhibit different sensitivities, with S= 24.6 for ZnO nanoplates and S= 14.1 for ZnO nanorods.

The dynamic response-recovery behaviors of the sensors fabricated from both ZnO hexagonal nanoplates and nanorods upon injection of different concentrations of EthOH are shown in Fig. 5b. Evidently, the output voltages of both ZnO sensors increase as EthOH is introduced into the test chamber but gradually decrease as the sensors are exposed to air, and such behavior is consistent with that of an *n*-type semiconducting gas sensor. However, it is clear that the increase in the output voltage upon exposure to EthOH is greater for ZnO nanoplates than for ZnO nanorods, indicating the higher sensitivity of the nanoplates. The response and recovery times of the two ZnO sensing materials toward different concentrations of EthOH are shown in Fig. 5c. Clearly, the ZnO hexagonal nanoplates exhibit faster response times than the ZnO nanorods, however, the recovery times of the nanoplates are slightly longer than those of the nanorods, due to the stronger interaction with EthOH, and hence more time is needed to return to the initial state.

Physical Chemistry Chemical Physics Accepted Manuscript

The changes in sensitivities of ZnO nanoplates and nanorods upon exposure to different amounts of EthOH are shown in Fig 5d. 5. It can be observed from this figure that the sensitivity always increases with increasing EthOH concentration for both ZnO nanostructures, and that the sensitivity of the ZnO hexagonal nanoplates is almost twice of that of the nanorods, with S_{plates}= 48 vs. S_{rods} = 28.1, at an EthOH concentration of 500 ppm. Aside from sensitivity and response-recovery behaviors, the stabilities of the two ZnO sensing materials were also assessed toward 100 ppm of EthOH at the working temperature of 300 °C, over 7 days. The results in Fig. 6 confirm that both ZnO nanostructures are highly stable sensor materials, with only minor changes in their sensitivities from 23.7-27.5 for ZnO nanoplates and 13.3-16.2 for ZnO nanorods, respectively. The average *S* value of the ZnO nanoplates over the 7-day period is 25, with a standard deviation of 1.43, whereas the average *S* value of the ZnO nanorods over the 7-day period is 15.2, with a standard deviation of 1.05.

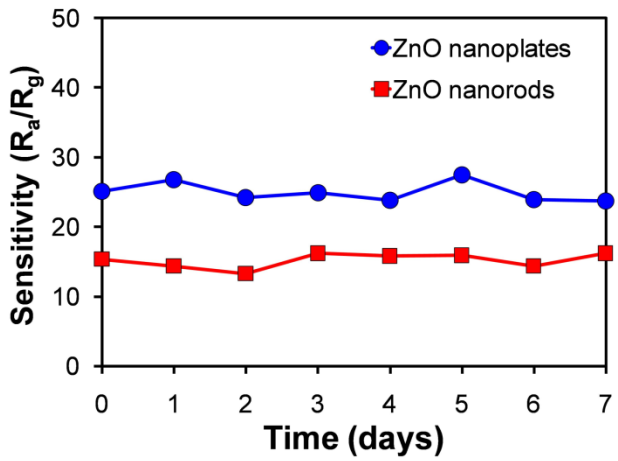

Fig. 6 Stability evaluations of the as-prepared ZnO sensing materials toward 100 ppm of EthOH over a testing period of 7 days.

The gas-sensing mechanism of these ZnO sensors is based on the changes in their resistance upon introduction of EthOH caused by the adsorption-desorption of the EthOH molecules on their surfaces.[31, 32] In air, oxygen (O_2) molecules adsorb on the surface of ZnO and ionize to form ionic oxygen species

Physical Chemistry Chemical Physics Accepted Manuscript

(mainly O^- at 300 °C) by capturing electrons from the conduction band of ZnO.[33] Such reactions lead to the formation of a thick space charge layer which increases the potential barrier, and ultimately increases the resistance of the ZnO sensor. However, when the ZnO sensor is exposed to EthOH, the EthOH molecules interact with the chemisorbed oxygen species (O^-) on the surface of the ZnO to form CO_2 and H_2O and release the trapped electrons back into the conduction band of ZnO, according to the equation:

$$C_2H_5OH\ (ads) + 6O^- \rightarrow 2CO_2\ (gas) + 3H_2O\ (gas) + 6e^- \quad (2)$$

This process increases in the carrier concentration, which consequently decreases the overall resistance of the ZnO sensor.

The above results clearly show that in the gas-sensing performance of ZnO nanostructures is highly dependent on the surface properties. Surface area is one of the most important factors affecting the sensitivity of metal oxide gas sensors. The larger the surface area, the more adsorption sites are available for the adsorption of O_2 molecules on the surfaces of the nanostructures, and therefore the higher the sensitivity. Moreover, besides the surface area, the highly exposed (0001) crystal surfaces of the ZnO nanoplates may also play an important role in enhancing their sensitivity toward EthOH. To further understand the sensing mechanism and to compare the EthOH adsorption capabilities of different ZnO crystal planes, we have carried out theoretical (DFT) simulations on the three main ZnO crystal planes: ZnO(0001), $(11\bar{2}0)$ and $(10\bar{1}0)$, as described in the following context.

3.4 DFT simulation

To further support the experimental results, DFT simulation method was used to simulate the adsorption behavior of EthOH molecules on ZnO$(10\bar{1}0)$, $(11\bar{2}0)$ and (0001) crystal planes, modified with adsorbed O^- ions, which are commonly found at high operating temperatures (≥ 300 °C).[34, 35] The modification

Physical Chemistry Chemical Physics Accepted Manuscript

with other adsorbed oxygen species such as O^{2-} or O_2^- might be possible, but the DFT simulation results show extremely low or extremely high energies for these cases (and they also do not converge), which possibly suggests that O^- is the most stable configuration for oxygen species in a typical gas-sensing experiment. Scheme 1a shows the side view and top view of the three surfaces of ZnO. These were firstly optimized, and then the EthOH molecule was placed on each surface during the simulations.

Table 2 Summary of calculated bond distances and adsorption energy

		Gas Phase	Surface		
			$10\bar{1}0$	$11\bar{2}0$	0001
Bond Distance/Angle	**O-H_1 (Å)**	0.977	1.020	1.040	1.695
	C_1-H_2(Å)	1.098	1.099	1.102	1.109
	C_1-O(Å)	1.438	1.449	1.442	1.406
	C_1-C_2(Å)	1.513	1.513	1.514	1.518
	H_1-O-C_1(°)	108.6	111.5	112.1	125.3
	O-C_1-C_2(°)	108.0	110.9	111.6	115.8
	O_{EthOH}-Zn_{ZnO} (Å)	-	2.118	2.051	1.937
	H_1-O^-_{ZnO} (Å)	-	1.679	1.499	1.05
	$E_{adsorption}$ (eV)	-	-1.12	-1.36	-5.72

Table 2 shows the bond distances between various atoms, the bond angles of the EthOH molecule before and after adsorption and the adsorption energies on O^- modified ZnO($10\bar{1}0$), ($11\bar{2}0$) and (0001) crystal planes. The DFT calculation performed for free EthOH molecule shows that it exhibits bond distances of 0.977, 1.098, 1.438, and 1.513 Å, corresponding to O-H, C-H, C-O, and C-C bonds, respectively. The results obtained via CASTEP are consistent with the reported theoretical results,[36, 37] and experimental results[38]. As the EthOH molecule approaches the O^- adsorbed ZnO surface, the O(EthOH) atom forms a bond with the surface Zn atom. The H(EthOH) atom will also form a bond with the O^-, mainly in the

Physical Chemistry Chemical Physics Accepted Manuscript

form of hydrogen bond. The DFT calculations indicate that the distance between H(EthOH) and O^- on ZnO(0001) surface is the smallest (1.05 Å), as shown in Table 2. This value is smaller than the reported value of 1.464 Å by Yuan et al[19], due to the addition of O^- in our present simulation. Furthermore, from Table 2, it can be observed that the O-H bond distance of the EthOH molecule stretches following its interactions with the surface Zn atoms. The greatest elongation of the O-H bond of EthOH molecule is found to be on the ZnO(0001) crystal plane, where the O-H bond distance increases from 0.977 to 1.695 Å.

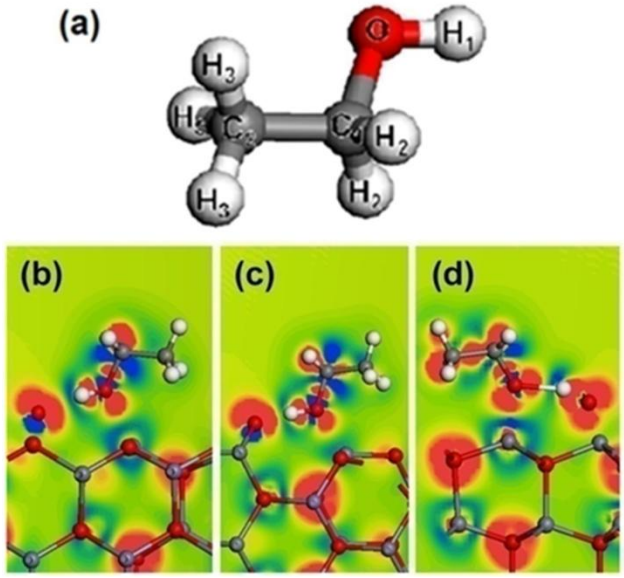

Fig. 7 (a) Free EthOH molecule (red atoms, grey atoms and white atoms represent O, C and H, respectively). Slice view of the electron density difference of EthOH adsorbed on O^- modified: (b) ZnO($10\bar{1}0$), (c) ZnO($11\bar{2}0$), and (d) ZnO(0001) crystal planes.

The stronger adsorption of EthOH molecule on ZnO(0001) leads to a great elongation of the O-H bond, similar to that observed on the $LaFeO_3$ (010) surface.[39] This can be confirmed by the Mulliken charges of related atoms, as listed in Table 3. After adsorption, the Mulliken charge of O^- ion on the ZnO(0001) surface is about −0.84 e, the lowest among three ZnO surfaces, suggesting that a strong interaction exists

Physical Chemistry Chemical Physics Accepted Manuscript

between the O^- ion and H(EthOH). In fact, the Mulliken charge of O(EthOH) is −0.65 e, which is greater than that of the O^- ion (-0.84 e), indicating that H(EthOH) has been dissociated from the molecule. In addition, the C-C-O and C-O-H angles of the EthOH molecule (Fig. 7a) also change compared to the free EthOH molecule, as shown in Table 2. Similar to the changes in bond distances, the most significant changes in bond angles occur when the EthOH molecule is adsorbed on the ZnO(0001) crystal plane, where the C_1-C_2-O an C_1-O-H_1 angles change from 108.0 and 108.6° to 125.3 and 115.8°, respectively.

Table 3 Mulliken charge (e) of O^- ion, H(EthOH) and O(EthOH) after EthOH adsorption

Mulliken charge	**Surface**		
	$\mathbf{10\bar{1}0}$	$\mathbf{11\bar{2}0}$	**0001**
O^- ion	-0.50	-0.50	-0.84
H(EthOH)	0.38	0.38	0.37
O(EthOH)	-0.65	-0.66	-0.65

The above analysis reveals that the strongest interaction occurs on the ZnO(0001) surface compared to the other ZnO surfaces. This is further confirmed by the calculation of the adsorption energies (E_{ads}), where the ZnO(0001) surface is found to exhibit the strongest adsorption energy of -5.72 eV after the interaction with EthOH. This implies that exposed (0001) crystal planes of the ZnO nanoplates promote better ethanol adsorption and therefore, higher sensitivity.

Further insights into the bonding mechanisms between EthOH molecule and the ZnO crystal planes are obtained by analyzing the density of states (DOS) of the adsorbed EthOH molecule, adsorbed O^- ion and surface Zn and O atoms. Fig. 8 shows the DOS of the EthOH molecule before (a) and after

Physical Chemistry Chemical Physics Accepted Manuscript

adsorption (d) on the ZnO(0001) surface. The gap between the lowest-unoccupied molecular orbital (LUMO) and the highest occupied molecular orbital (HOMO) gap is 4.5 eV, as shown in Fig. 8a. Fig. 8b shows the PDOS plots of the surface O2*p* orbital and Zn3*d* orbital. The obtained PDOS results are in good agreement with the report of Breedon et al.[18] who demonstrated that the *p* orbitals of the surface oxygen are mainly located at a higher energy range (−4.0 eV to Fermi energy level), while at a lower energy range (−6.0 eV to −4.0 eV), the hybridization is mainly caused by the Zn3*d* orbitals and EthOH molecular orbitals. These results imply that the adsorbed oxygen species on the surface of the ZnO play an important role in the gas adsorption process, which is in accordance with a previous DFT study on the adsorption of EthOH on SnO_2 (110) surface.[40] Fig. 8c shows the DOS of the adsorbed O^- ion and it is clear that strong hybridization occurs between the O^- ion and HOMO, HOMO-1 molecular orbitals of EthOH. This suggests that the adsorbed O^- ion plays an important role in the adsorption of EthOH on ZnO crystal planes.

For further confirmation, the DOS of the EthOH molecule adsorbed on O^- modified ZnO(0001), $(10\bar{1}0)$ and $(11\bar{2}0)$ crystal planes were analyzed, as shown in Fig. 9. It is observed that after adsorption, the DOS of the EthOH molecule are broadened due to the strong hybridization with the adsorbed O^- ion. The DOS of the adsorbed EthOH molecule on the three ZnO crystal planes are quite different to that of the free EthOH molecule. This indicates that the electron densities within the EthOH molecule are changed in the adsorption process. The strong interaction between the adsorbed O^- ion and H(EthOH) atom results in the shifting and broadening of DOS peaks of the adsorbed EthOH molecule, suggesting a chemical adsorption. The broadening of the orbitals has also been reported on rutile TiO_2(110) surfaces.[41] The DOS of EthOH molecule after adsorption on ZnO(0001) surface becomes broaden and

Physical Chemistry Chemical Physics Accepted Manuscript

the HOMO-1 molecular orbital of EthOH shifts upward, indicating the occurrence of strong orbital hybridization.

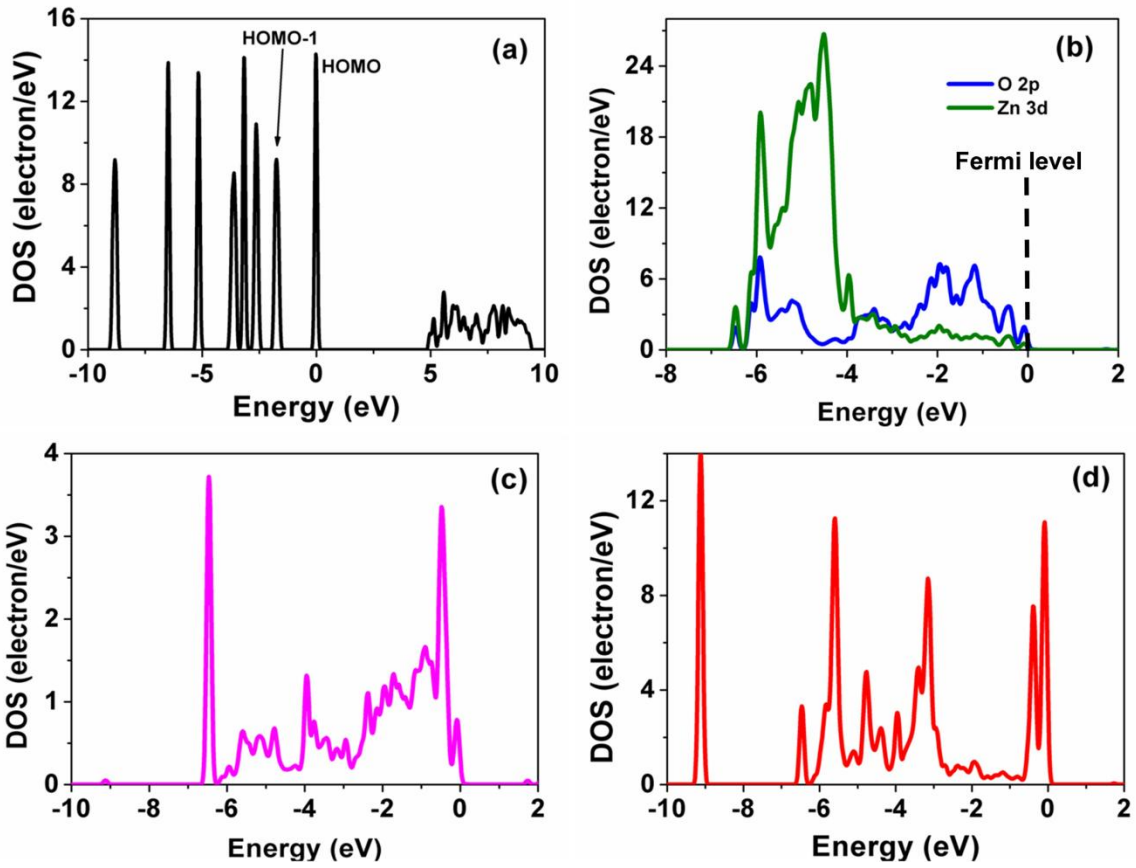

Fig. 8 (a) Total DOS plot of a single EthOH molecule; (b) PDOS plots of the surface oxygen 2*p* (O2*p*) and zinc 3*d* (Zn3*d*) orbitals on the ZnO(0001) surface; (c) PDOS plot of adsorbed O^- ion on the ZnO(0001) surface; (d) total DOS plot of the EthOH molecule after adsorption.

In comparison, the DOS of EthOH molecule adsorbed on O^- modified ZnO($10\bar{1}0$) and ($11\bar{2}0$) crystal planes are nearly identical, with the HOMO molecular orbital shifting downward and becoming weaker. However, the HOMO molecular orbital of EthOH molecule adsorbed on the ($11\bar{2}0$) plane is slightly higher than that adsorbed on the ZnO($10\bar{1}0$) plane, indicating a slightly stronger hybridization on the ZnO($11\bar{2}0$) plane. The above analysis provides the following insights regarding the ethanol-sensing

Physical Chemistry Chemical Physics Accepted Manuscript

mechanism of ZnO sensor: (i) the adsorption of EthOH on ZnO surface is mainly caused by the strong interaction between adsorbed O^- ion and H(EthOH) atom, (ii) strong hybridization occurs between the adsorbed O^- ion and the HOMO, HOMO-1 molecular orbitals and this is the main driving force for surface reactions, and (iii) the ZnO(0001) crystal plane shows a higher adsorption capability for EthOH than the ZnO($10\bar{1}0$) and ($11\bar{2}0$) planes.

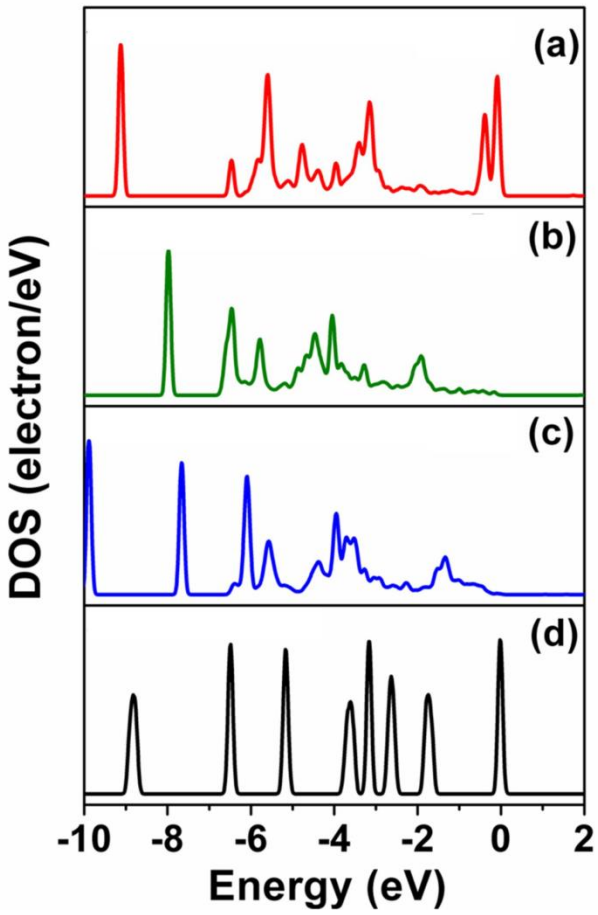

Fig. 9 Total DOS plots of EthOH molecule adsorbed on O^- modified (a) ZnO(0001), (b) ZnO($10\bar{1}0$), and (c) ZnO($11\bar{2}0$); (d) total DOS plot of free EthOH molecule.

Physical Chemistry Chemical Physics Accepted Manuscript

4. Conclusions

In this study, we have demonstrated facile solvothermal methods for the synthesis of ZnO nanoplates and nanorods with exposed (0001) and $(10\bar{1}0)$ crystal planes, respectively. The gas-sensing results show that ZnO hexagonal nanoplates exhibit two times higher sensitivity toward EthOH than the ZnO nanorods under a similar optimum operating temperature of 300 °C. This could be contributed to two main factors based on the experimental findings: one is the larger surface area of the nanoplates compared to the nanorods (14.4 m^2/g vs. 7.43 m^2/g) and another is the exposed (0001) planes of the nanoplates. To confirm the beneficial effect of the exposed (0001) planes, DFT simulations were used to quantify the ethanol adsorption on O^- modified ZnO(0001), $(10\bar{1}0)$, and $(11\bar{2}0)$ crystal surfaces. The results reveal that the exposed (0001) crystal planes of the ZnO nanoplates show: (i) stronger adsorption energy (-5.72 eV on ZnO(0001) plane vs. -1.12 eV on ZnO$(10\bar{1}0)$ plane) and (ii) stronger hybridization between the adsorbed O*2p* orbital and the HOMO, HOMO-1 molecular orbitals, suggesting a stronger adsorption of EthOH molecules adsorbed on the ZnO(0001) plane. The combined experimental and theoretical results may provide new insights into the crystal plane-dependent gas-sensing performance of metal oxide gas sensors. Furthermore these findings will be useful for designing and constructing novel nanostructures with specifically exposed crystal planes for surface-related applications such as gas sensors and catalysis.

Acknowledgements

We gratefully acknowledge the financial support of the Australian Research Council (ARC) projects. The authors also acknowledge access to the UNSW node of the Australian Microscopy and Microanalysis Research Facilities (AMMRF). The authors thank Dr. Jason Scott of Particle Catalysis (PARTCAT) group for the assistance with the BET measurements.

Physical Chemistry Chemical Physics Accepted Manuscript

Physical Chemistry Chemical Physics Accepted Manuscript

References

1. E. Hosono, S. Fujihara, I. Honma and H. Zhou, *Adv. Mater.*, 2005, **17**, 2091-2094.

2. M. H. Huang, S. Mao, H. Feick, H. Yan, Y. Wu, H. Kind, E. Weber, R. Russo and P. Yang, *Science*, 2001, **292**, 1897-1899.

3. Z. L. Wang and J. Song, *Science*, 2006, **312**, 242-246.

4. A. Sinhamahapatra, A. K. Giri, P. Pal, S. K. Pahari, H. C. Bajaj and A. B. Panda, *J. Mater. Chem.*, 2012, **22**, 17227-17235.

5. J.-Y. Dong, C.-H. Lin, Y.-J. Hsu, S.-Y. Lu and D. S.-H. Wong, *CrystEngComm*, 2012, **14**, 4732-4737.

6. G. Korotcenkov, *Mat. Sci. Eng. B*, 2007, **139**, 1-23.

7. P. Song, Q. Wang and Z. Yang, *Sens Actuators B*, 2012, **168**, 421-428.

8. C. Wang, L. Yin, L. Zhang, Y. Qi, N. Lun and N. Liu, *Langmuir*, 2010, **26**, 12841-12848.

9. D. Su, H. Fu, X. Jiang and G. Wang, *Sens. Actuators, B*, 2013, **186**, 286-292.

10. Z. Lai, F. Peng, H. Wang, H. Yu, S. Zhang and H. Zhao, *J. Mater. Chem. A*, 2013, **1**, 4182-4185.

11. H. Men, P. Gao, B. Zhou, Y. Chen, C. Zhu, G. Xiao, L. Wang and M. Zhang, *Chem. Commun.*, 2010, **46**, 7581-7583.

12. D. Bao, P. Gao, L. Wang, Y. Wang, Y. Chen, G. Chen, G. Li, C. Chang and W. Qin, *ChemPlusChem*, 2013, **78**, 1266-1272.

13. X. Han, X. Han, L. Li and C. Wang, *New. J. Chem.*, 2012, **36**, 2205-2208.

14. M. Breedon, M. J. S. Spencer and I. Yarovsky, *Surf. Sci.*, 2009, **603**, 3389-3399.

15. M. J. S. Spencer, K. W. J. Wong and I. Yarovsky, *Mater. Chem. Phys.*, 2010, **119**, 505-514.

16. J. D. Prades, A. Cirera and J. R. Morante, *Sens. Actuators, B*, 2009, **142**, 179-184.

17. W. An, X. Wu and X. C. Zeng, *J. Phys. Chem. C*, 2008, **112**, 5747-5755.

18. M. Breedon, M. J. S. Spencer and I. Yarovsky, *J. Phys. Chem. C*, 2010, **114**, 16603-16610.

19. Q. Yuan, Y.-P. Zhao, L. Li and T. Wang, *J. Phys. Chem. C*, 2009, **113**, 6107-6113.

20. Y. V. Kaneti, J. Yue, X. Jiang and A. Yu, *J. Phys. Chem. C*, 2013, **117**, 13153-13162.

21. Z. Li, W. Pan, D. Zhang and J. Zhan, *Chem. Asian. J*, 2010, **5**, 1854-1859.

22. S. J. Clark, M. D. Segall, C. J. Pickard, P. J. Hasnip, M. I. J. Probert, K. Refson and M. C. Payne, *Z. Kristallogr.*, 2005, **220**, 567-570.

23. X.-G. Han, H.-Z. He, Q. Kuang, X. Zhou, X.-H. Zhang, T. Xu, Z.-X. Xie and L.-S. Zheng, *J. Phys. Chem. C*, 2008, **113**, 584-589.

24. Y. Ding, P. X. Gao and Z. L. Wang, *J. Am. Cer. Soc.*, 2004, **126**, 2066-2072.

25. J. Y. Lao, J. G. Wen and Z. F. Ren, *Nano Lett.*, 2002, **2**, 1287-1291.

26. R. Shi, P. Yang, X. Dong, Q. Ma and A. Zhang, *Appl. Surf. Sci.*, 2013, **264**, 162-170.

27. B. Li and Y. Wang, *J. Phys. Chem. C*, 2009, **114**, 890-896.

28. B. Cao and W. Cai, *J. Phys. Chem. C*, 2007, **112**, 680-685.

29. Y. Chang, J. Xu, Y. Zhang, S. Ma, L. Xin, L. Zhu and C. Xu, *J. Phys. Chem. C*, 2009, **113**, 18761-18767.

30. J. Huang, Y. Wu, C. Gu, M. Zhai, K. Yu, M. Yang and J. Liu, *Sens. Actuators, B*, 2010, **146**, 206-212.

31. Z. Yang, L.-M. Li, Q. Wan, Q.-H. Liu and T.-H. Wang, *Sens. Actuators, B*, 2008, **135**, 57-60.

32. Z. Jing and J. Zhan, *Adv. Mater.*, 2008, **20**, 4547-4551.

33. J. Xu, Y. Li, H. Huang, Y. Zhu, Z. Wang, Z. Xie, X. Wang, D. Chen and G. Shen, *J. Mater. Chem.*, 2011, **21**, 19086-19092.

34. T. Santhaveesuk, D. Wongratanaphisan and S. Choopun, *Sens. Actuators, B*, 2010, **147**, 502-507.

35. M. Iwamoto, Y. Yoda, N. Yamazoe and T. Seiyama, *J. Phys. Chem.*, 1978, **82**, 2564-2570.

Physical Chemistry Chemical Physics Accepted Manuscript

36. W. Wang, C. Zhu and Y. Cao, *Int. J. Hydrogen Energ.*, 2010, **35**, 1951-1956.

37. N. I. Butkovskaya, Y. Zhao and D. W. Setser, *J. Phys. Chem.*, 1994, **98**, 10779-10786.

38. G. F. Bauerfeldt, L. M. M. De Albuquerque, G. Arbilla and E. C. Da Silva, *J. Mol. Struct-Theochem.*, 2002, **580**, 147-160.

39. X. Liu, B. Cheng, J. Hu and H. Qin, *Comp. Mater. Sci.*, 2013, **68**, 90-94.

40. J. Yue, X. Jiang and A. Yu, *J. Phys. Chem. C*, 2013, **117**, 9962-9969.

41. J. N. Muir, Y. Choi and H. Idriss, *Phys. Chem. Chem. Phys.*, 2012, **14**, 11910-11919.

Physical Chemistry Chemical Physics Accepted Manuscript